nature geoscience

Article

https://doi.org/10.1038/s41561-025-01893-z

High normal stress promoted supershear rupture during the 2023 M_w 7.8 Kahramanmaraş earthquake

Received: 24 May 2024

Accepted: 25 November 2025

Published online: 06 January 2026

Check for updates

Jing Chen[1], Mijian Xu[1], Yiming Bai[1], Shucheng Wu[2], Xiao Xiao[1], Shijie Hao[1], Masaru Nagaso[1], Hongfeng Yang[3] & Ping Tong[1,4]

On 6 February 2023, two major earthquakes with moment magnitude (M_w) of 7.8 and 7.6 ruptured multiple segments of the Eastern Anatolian Fault system, resulting in many casualties and extensive property damage in Turkey and Syria. The M_w 7.8 earthquake involved bilateral rupture along the Eastern Anatolian Fault, with at least partially supershear rupture towards the northeast and subshear rupture towards the southwest. The cause of this difference in rupture speed remains debated. Here we present evidence from seismic tomographic imaging linking this difference to structural and stress variations along the fault. Specifically, a low-velocity anomaly and a fault-parallel fast velocity direction of anisotropy in the southwest Amanos–Pazarcık segment suggest fluid infiltration, which could facilitate fault creep and reduce the stress loading rate. By contrast, the Erkenek segment to the northeast is associated with a high-velocity anomaly and fault-normal fast velocity direction, suggesting limited fluid infiltration and increased stress accumulation. Hence, we propose that the contrast in stress accumulation explains the discrepancy in rupture speeds in this earthquake and that fault structure in addition to stress loading may influence stress accumulation and thus whether a fault ruptures at supershear speeds.

On 6 February 2023, two major earthquakes with moment magnitude (M_w) of 7.8 and 7.6 ruptured the Eastern Anatolian Fault (EAF) system, resulting in more than 50,000 deaths in Turkey and Syria and total losses exceeding US$100 billion (refs. 1,2). In this study, we focus on the nucleation and rupture behaviour of the M_w 7.8 earthquake that triggered the catastrophe. Numerous geophysical studies have simulated the rupture process of the M_w 7.8 earthquake by analysing seismic waveforms, global navigation satellite system (GNSS) data and/or interferometric synthetic aperture radar (InSAR) data[1,3–11]. These studies show that this earthquake originated at the Nurdağı–Pazarcık Fault and propagated northeastwards to the junction with the EAF, leading to a bilateral rupture along the EAF (Fig. 1). The forward rupture traversed the northeastern part of the Pazarcık segment and the Erkenek segment, before being arrested at the western margin of the Pütürge segment. The backward rupture propagated southwestwards through the southeastern part of the Pazarcık segment and the Amanos segment. The backward rupture speed is reported to be overall subshear[1,3–11], accompanied by possible transient supershear rupture[7–11]. However, the estimated forward rupture speed exhibits variability. Specifically, the first-order model of Gabriel et al.[3], constrained by seismic and geodetic

[1]Division of Mathematical Sciences, School of Physical and Mathematical Sciences, Nanyang Technological University, Singapore, Singapore. [2]State Key Laboratory of Geological Processes and Mineral Resources, China University of Geosciences, Wuhan, China. [3]Department of Earth and Environmental Sciences, The Chinese University of Hong Kong, Hong Kong, China. [4]Earth Observatory of Singapore, Nanyang Technological University, Singapore, Singapore.
e-mail: tongping@ntu.edu.sg

https://doi.org/10.1038/s41561-025-01893-z

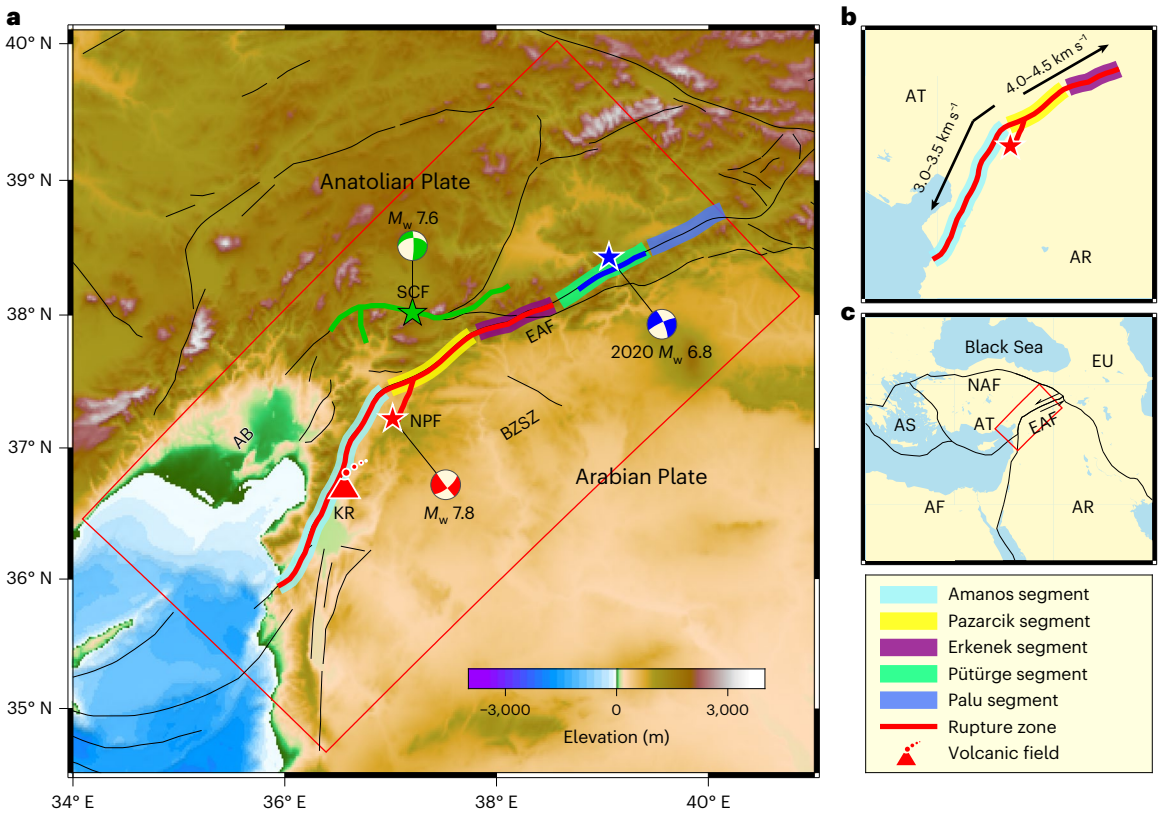

Fig. 1 | Overview map of the EAF system. a, Major faults and tectonic boundaries are represented by black lines. The 2020 M_w 6.8, 2023 M_w 7.8 and 2023 M_w 7.6 earthquakes are indicated by blue, red and green stars, respectively, with their rupture zones delineated by thick lines in the corresponding colours. Various segments of the EAF are highlighted in different colours. Our study region is outlined by the oblique red box. AB, Adana Basin; BZSZ, Bitlis–Zagros Suture zone; EAF, Eastern Anatolian Fault; KR, Karasu Rift volcanic field; NPF, Nurdağı–Pazarcık Fault; SCF, Savrun–Cardak Fault. **b**, Bilateral rupture along the EAF of the M_w 7.8 earthquake. The rupture speeds are estimated as described previously[1]. **c**, Broader view of the study region, with black lines denoting plate boundaries. AF, African Plate; AR, Arabian Plate; AS, Aegean Sea; AT, Anatolian Plate; EU, Eurasian Plate; NAF, North Anatolian Fault. Basemaps generated with Generic Mapping Tools[64].

observations available within days of the sequence, indicates a subshear rupture speed, supported by estimated values not exceeding ~3.2 km s^{-1} (refs. 4–6). By contrast, supershear rupture speeds have also been suggested for the forward rupture[1,9,10] or confined to the Pazarcık segment[7,8]. As noted by Ren et al.[1], the discrepancy in rupture speeds may be attributed to differences in the inversion datasets and model parameterizations. By jointly inverting multiple datasets with direct waveform analyses, Ren et al.[1] developed an improved kinematic model, showing that the forward rupture propagated at supershear speeds of 4.0–4.5 km s^{-1}, faster than the 3.0–3.5 km s^{-1} estimated for the backward rupture. This phenomenon, characterized by rupture propagation velocity exceeding the shear wave velocity, typically leads to intensified ground shaking, posing severe seismic hazards. Although numerous studies have investigated supershear rupture[12–16], the underlying mechanisms remain elusive and warrant further investigation. The contrast in rupture speed of the M_w 7.8 event along the EAF presents a valuable opportunity to gain key insights into the contributing factors of supershear rupture.

The EAF is a typical left-lateral strike-slip fault, separating the Anatolian microplate to the northwest from the Arabian Plate to the southeast[17] (Fig. 1). This fault accommodates the westward extrusion of the Anatolian Plate in response to the northward collision of the Arabian Plate[18]. Various studies have reported substantial variations in subsurface properties across the rupture zone of the M_w 7.8 earthquake encompassing the Amanos, Pazarcık and Erkenek segments. For instance, Güvercin et al.[19] observed a pronounced decrease in seismic activity along the EAF from northeast to southwest (Extended Data Figs. 1 and 2). They also reported that the majority of earthquakes in the Amanos segment display focal mechanisms with normal components, whereas those in the Erkenek segment show reverse components (Extended Data Fig. 3). The variations in focal mechanisms are consistent with the geodesy-derived strain rate field[20], revealing positive and negative dilatation rates within the Amanos and Erkenek segments, respectively (Extended Data Fig. 3). Moreover, GPS observations suggest a long-term average fault slip rate of ~10 mm per year in the Pazarcık and Erkenek segments, in contrast to a notably lower slip rate of ~4.5 mm per year in the Amanos segment[18,21]. These observations indicate structural and stress variations in the rupture zone, which may be associated with the contrast in rupture speeds that warrants further investigation.

Seismic velocity and anisotropy are intrinsic rock properties that provide insights into subsurface structure and stress. Seismic velocity is closely related to the compositional and thermal characteristics of subsurface rocks and the presence of fluids, aiding in the understanding of earthquake nucleation[22–24]. Additionally, seismic anisotropy describes the dependence of wave speed on propagation direction. Its mechanism in the crust is typically categorized into stress-induced and structure-induced anisotropy[25,26], associated with multiple factors such as fracture opening and closure[27], stress-strain fields[28] and oriented arrangement of mineral crystals[29,30]. The ability to reflect subsurface structure and stress makes seismic anisotropy a promising indicator for analysing earthquake rupture behaviour[31,32]. Previous studies have conducted seismic tomography[33–40] in and around the rupture zone. However, these investigations either lack information on seismic anisotropy or focus on the entire Anatolian region, thus providing limited structural constraints on the rupture behaviour of

https://doi.org/10.1038/s41561-025-01893-z

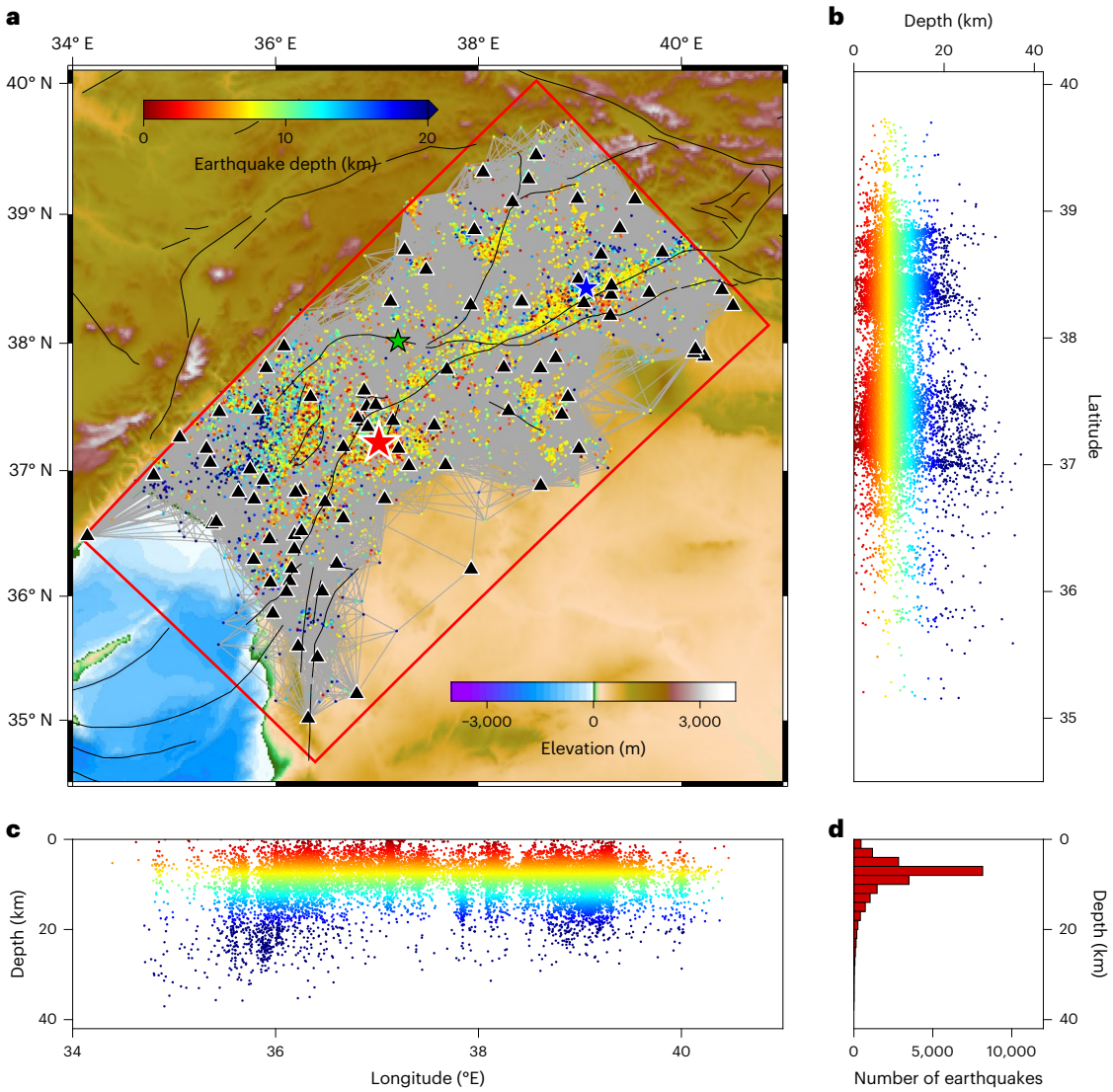

Fig. 2 | The spatial distribution of earthquakes and seismic stations within the study region. a, Earthquakes and stations projected onto the horizontal map. Earthquakes are denoted by dots, colour-coded by focal depths. Seismic stations are represented by black triangles. Each travel time is depicted as a grey line connecting the associated earthquake and seismic station. **b**,**c**, Earthquakes and stations projected onto vertical sections. **d**, Number of earthquakes at different depth ranges, showing that the most earthquakes occur above 20 km depth. Station and earthquake location data from ref. 65. Basemap in **a** generated with Generic Mapping Tools[64].

the M_w 7.8 earthquake. To close this observation gap and explore the relationship between subsurface structures and the distinctive rupture behaviour, we determine the P-wave velocity and azimuthal anisotropy beneath the entire rupture zone by applying the adjoint-state travel time tomography (ATT) method[41–43] to first P-wave arrival times and common-source differential arrival times (Fig. 2).

Along-fault structural and anisotropic variations

Our tomographic images reveal several pronounced crustal velocity anomalies around the EAF. At 5-km depth (Fig. 3a), the velocity model closely corresponds to surface geology. The Adana Basin is characterized by a low-velocity anomaly labelled as L1. Additionally, a broad low-velocity anomaly labelled as L2 is evident beneath the Bitlis–Zagros Suture zone. From depths of 10 to 15 km, the seismic velocity along the EAF exhibits diverse patterns from southwest to northeast (Fig. 3b,c). Specifically, a −4% low-velocity anomaly labelled as L3 is imaged beneath the Amanos and Pazarcık segments. This anomaly is bounded to the northeast by a +2% high-velocity perturbation (H2) beneath the Erkenek segment. Further northeast, the Pütürge segment separates a +4% high-velocity anomaly (H1) from a −4% low-velocity anomaly (L4) at 10-km depth. This velocity contrast evolves into a broad low-velocity body (L4) at greater depths.

The crustal azimuthal anisotropy in the rupture zone exhibits a nearly consistent pattern across various depths, with an amplitude of approximately 4% at 10-km depth (Fig. 3d–f). The fast velocity direction (FVD) closely aligns with the fault in the Amanos segment and the southwestern part of the Pazarcık segment (A1). This fault-parallel FVD gradually transitions into a fault-normal direction in the Erkenek segment (A2). Moving further northeast, in the Pütürge segment, pronounced azimuthal anisotropy (A3) with a high angle to the fault strike is observed within the region of L4. Conversely, azimuthal anisotropy is relatively weak within the region of H1.

Fluid infiltration in the Amanos–Pazarcık segment

We proposed that the observed L3 (Fig. 4d) in the Amanos–Pazarcık segment indicates crustal melting beneath the Karasu Rift. This hypothesis finds support in the high surface heat flow exceeding 80 mW m^{-2} in that region[44] (Extended Data Fig. 4), and the exposed Quaternary

https://doi.org/10.1038/s41561-025-01893-z

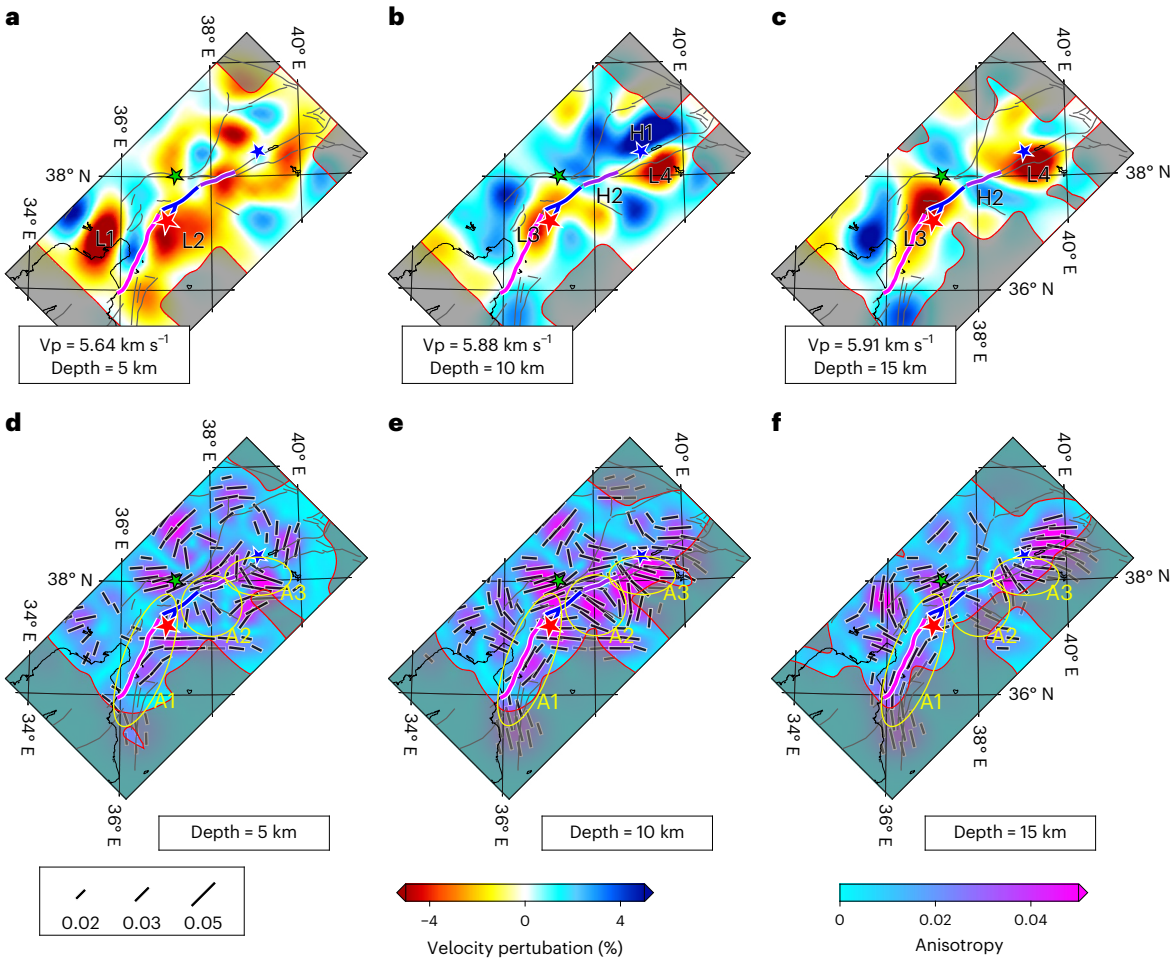

Fig. 3 | Horizontal sections of the imaging results. The Amanos, Pazarcık and Erkenek segments of EAF are highlighted by thick magenta, blue and purple lines. Major faults and tectonic boundaries are shown in grey lines. The 2020 M_w 6.7, 2023 M_w 7.8 and 2023 M_w 7.6 earthquakes are indicated by blue, red and green stars, respectively. **a**–**c**, Velocity perturbations relative to the horizontal average at depths of 5 km (**c**), 10 km (**d**) and 15 km (**e**), with prominent anomalies labelled. Vp denotes the horizontal average of P-wave velocity. The well-resolved region is delineated by the red curve, determined by the checkerboard resolution test (Supplementary Fig. 4). **d**–**f**, Azimuthal anisotropic models at depths of 5 km (**d**), 10 km (**e**) and 15 km (**f**). Black bars indicate azimuthal anisotropy, with length and direction denoting magnitude and fast velocity direction. Bars with magnitudes smaller than 0.015 are omitted. Anisotropic anomalies near the rupture zone are highlighted and labelled. Basemaps generated with Generic Mapping Tools[64].

basalts (1.6–0.05 Ma) in the Karasu volcanic field[45], originating from asthenospheric mantle upwelling[46,47] (Fig. 4c,d). As an active fault, the EAF accommodates the relative movement between the Anatolian and Arabian plates and may provide a pathway for magma to traverse through the entire crust. The extensional regime in the Amanos segment, suggested by dilatational strain rates[20] and focal mechanisms with normal components[19] (Extended Data Fig. 3), may facilitate magma infiltration into the fault zone during its ascent to the surface (Fig. 4c,d).

Fluid infiltration into the fault zone maintains the opening of fractures by increasing pore pressure[27,48,49] (Fig. 4a), consequently leading to azimuthal anisotropy predominantly controlled by fault zone fractures. This is evidenced by the fault-parallel FVDs imaged in the Amanos segment and the southwestern part of the Pazarcık segment (Fig. 4d, A1). The elevated pore pressure weakens the fault frictional strength by reducing the effective normal stress (normal stress minus pore pressure), which may facilitate fault creep[50–55] and thereby result in decreased stress loading in the Amanos and southwestern Pazarcık segments. Recent statistics indicate fewer earthquakes along the Amanos and southwestern Pazarcık segments compared to the Erkenek segment[19] (Extended Data Figs. 1 and 2), despite comparable fault slip rates in the Pazarcık and Erkenek segments[21]. In addition to the lower slip rate in the Amanos segment, the reduction in seismicity may be also attributed to fault creep which accommodates a portion of fault slip budget aseismically[56].

Enhanced normal stress in the Erkenek segment

The FVDs of azimuthal anisotropy shift from fault-parallel in the Amanos segment to fault-normal in the Erkenek segment (Fig. 4d, A1 and A2), indicating that stress-induced anisotropy prevails over structure-induced anisotropy in the Erkenek segment. This transition corresponds to the local pattern of the strain rate tensor[20], which shifts from dilatational strain rate in the Amanos segment to compressional strain rate in the Erkenek segment (Extended Data Fig. 3). It is also supported by the focal mechanisms of earthquakes within the fault zone, with the majority exhibiting focal mechanisms with normal components in the Amanos segment but reverse components in the Erkenek segment[19] (Extended Data Fig. 3). These observations collectively suggest that the Erkenek segment may experience enhanced fault-normal stress compared to the Amanos segment. The high normal stress facilitates the closure of fault-related macro-fractures and microcracks parallel to the EAF, leading to the observed fault-normal FVDs[25] (Fig. 4b,d).

The heightened normal stress in the Erkenek segment also tends to reduce fracture permeability, inhibiting fluid infiltration into

https://doi.org/10.1038/s41561-025-01893-z

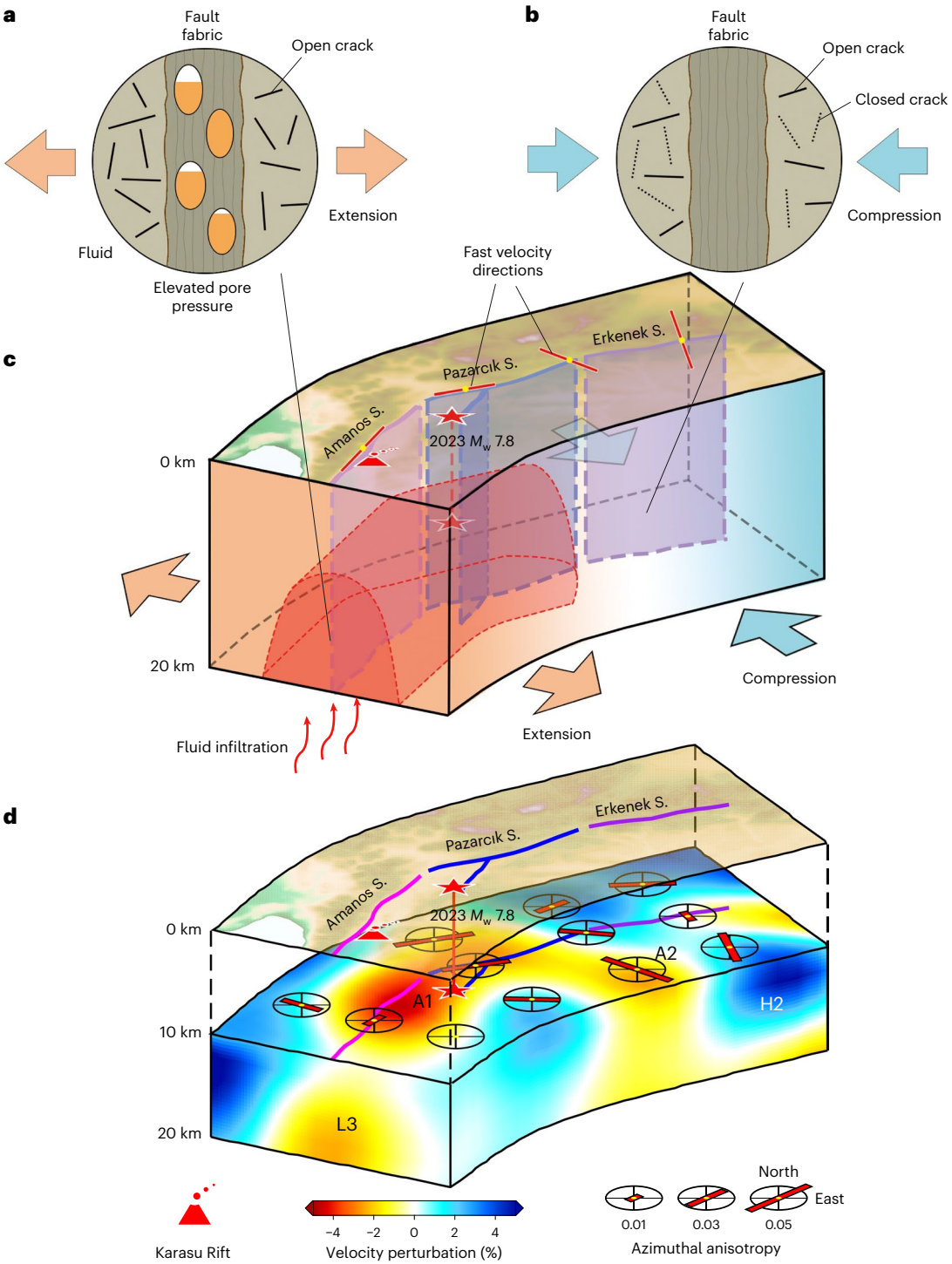

Fig. 4 | Cartoon illustrating the structure of the M_w 7.8 earthquake rupture zone. a,**b**, Fault structures with (**a**) and without (**b**) fluid infiltration, respectively. **c**,**d**, Conceptual cartoon (**c**) and corresponding imaging result (**d**) of the rupture zone. Notably, fluid infiltration in the Amanos and Pazarcık segments leads to contrasting fault structures compared to the Erkenek segment where fluid infiltration is inhibited. Further interpretation details are provided in the text. Maps in **c** and **d** generated with Generic Mapping Tools[64].

the fault zone[57]. The presence of H2 (Fig. 4c,d) coincides with the limited degree of fluid infiltration, resulting in low pore pressure. The enhanced normal stress, coupled with the low pore pressure, contributes to an increased effective normal stress. Consequently, elevated frictional strength inhibits fault creep[58], which may explain the higher seismicity observed in the Erkenek segment[19] (Extended Data Fig. 1). This suggests that high stress accumulation is favoured in the Erkenek segment.

Fault structural controls on rupture behaviour

The M_w 7.8 earthquake is located at the eastern margin of L3 (Fig. 3b). This area may represent a brittle-ductile transition zone, believed to facilitate stress accumulation[23,59], thus contributing to the earthquake nucleation. Subsequently, the earthquake triggers a bilateral rupture along the EAF. The backward rupture traverses through the southwestern termination of the EAF, whereas the forward rupture is arrested at the western margin of the Pütürge segment. This arrestation may be

attributed to the 2020 M_w 6.8 earthquake, which relieved stress in the Pütürge segment and prevented further northeast propagation of the 2023 M_w 7.8 earthquake rupture.

Notably, the bilateral rupture along the EAF exhibits contrasting behaviours. The backward rupture propagates southwestwards at overall subshear speeds, whereas the forward rupture traverses northeastwards at supershear speeds[1,6,9]. This discrepancy in rupture speed may be explained by a prevailing theory[14]: supershear rupture occurs when the seismic S ratio, expressed as $\frac{\tau_p-\tau_0}{\tau_0-\tau_r}$, falls below a critical threshold. In other words, for given peak strength τ_p and residual strength τ_r, a higher initial stress loading τ_0 favours supershear rupture[60–62]. Therefore, to rationalize the supershear rupture speed observed in the forward rupture, the Erkenek segment is expected to have a higher stress accumulation compared to the Amanos segment.

However, under a homogeneous structural model, the computed stress loading does not support the expected stress accumulation contrast between the Amanos and Erkenek segments. For instance, Nalbant et al.[63] computed stress accumulation along the EAF since 1822, considering fault slip for inter-seismic stress loading and historical large earthquakes ($M_w \geq 6.6$) for co-seismic stress loading. Their results show high stress accumulation in the Pazarcık segment due to high fault slip rates (10.3 mm per year) and a long period of seismic silence since the 1513 M_w 7.4 earthquake. In contrast, accumulation periods in the Amanos and Erkenek segments are shorter, starting from the 1822 M_w 7.5 earthquake and the 1893 M_w 7.1 earthquake, respectively. The fault slip rates in the Amanos and Erkenek segments are reported to be 4.5 mm per year and 10.5 mm per year (ref. 21), respectively. Considering the stress loading rate associated with fault slip rate and silence period, the stress accumulations in the Amanos and Erkenek segments should be comparable, but much lower than that in the Pazarcık segment[63]. This seems to contradict the expected stress loading difference between the Amanos and Erkenek segments. Additionally, Ren et al.[1] calculated the inter-seismic stress loading rate with homogeneous rock properties. The stress loading rate in the Erkenek segment is estimated to be 0.01 GPa per year, much lower than the rate needed for the released stress of the 2023 M_w 7.8 earthquake. Such a value requires an additional 80 years to accumulate sufficient prestress[1]. All the above indicates that there must be other factors influencing the shear stress loading along the fault zone.

Our tomographic results reveal substantial structural variations along the EAF suggesting that structural heterogeneity is non-negligible when estimating fault stress accumulation. In the Amanos and Pazarcık segments, the increased pore pressure arising from fluid infiltration weakens the fault and facilitates creep, potentially resulting in a lower stress loading rate than that estimated in a homogeneous structure. Despite fluid infiltration, the stress loading in the Pazarcık segment remains high due to the sufficiently long period for stress accumulation since the 1513 M_w 7.4 earthquake. In contrast, in the Erkenek segment, the heightened normal stress hinders fluid infiltration into the fault zone. The elevated effective normal stress, resulting from the enhanced normal stress and reduced pore pressure, strengthens the fault and inhibits fault creep, favouring high stress accumulation. By incorporating structural heterogeneity along the fault, we infer higher stress accumulation in the Pazarcık and Erkenek segments than in the Amanos segment. This stress pattern helps explain the supershear rupture speed observed in the forward rupture, emphasizing the structural controls on earthquake rupture behaviour.

Online content

Any methods, additional references, Nature Portfolio reporting summaries, source data, extended data, supplementary information, acknowledgements, peer review information; details of author contributions and competing interests; and statements of data and code availability are available at https://doi.org/10.1038/s41561-025-01893-z.

References

1. Ren, C. et al. Supershear triggering and cascading fault ruptures of the 2023 Kahramanmaraş, Türkiye, earthquake doublet. *Science* **383**, 305–311 (2024).
2. Liu, Y., Wang, Z. & Zhang, X. Estimating the final fatalities using early reported death count from the 2023 Kahramanmaraş, Türkiye, MS 8.0–7.9 earthquake doublet and revising the estimates over time. *Earthquake Res. Adv.* **5**, 100331 (2025).
3. Gabriel, A. A., Ulrich, T., Marchandon, M., Biemiller, J. & Rekoske, J. 3D dynamic rupture modeling of the 6 February 2023, Kahramanmaraş, Turkey M_w 7.8 and 7.7 earthquake doublet using early observations. *Seismic Rec.* **3**, 342–356 (2023).
4. Xu, L. et al. The overall-subshear and multi-segment rupture of the 2023 Mw7.8 Kahramanmaraş, Turkey earthquake in millennia supercycle. *Commun. Earth Environ.* **4**, 379 (2023).
5. Melgar, D. et al. Sub-and super-shear ruptures during the 2023 Mw 7.8 and Mw 7.6 earthquake doublet in SE Türkiye. *Seismica* **2**, v2i3.387 (2023).
6. Jia, Z. et al. The complex dynamics of the 2023 Kahramanmaraş, Turkey, M_w 7.8–7.7 earthquake doublet. *Science* **381**, 985–990 (2023).
7. Wang, Z. et al. Dynamic rupture process of the 2023 *Mw* 7.8 Kahramanmaraş earthquake (SE Türkiye): variable rupture speed and implications for seismic hazard. *Geophys. Res. Lett.* **50**, e2023GL104787 (2023).
8. Delouis, B., van den Ende, M. & Ampuero, J. P. Kinematic rupture model of the 6 February 2023 M_w 7.8 Türkiye earthquake from a large set of near-source strong-motion records combined with GNSS offsets reveals intermittent supershear rupture. *Bull. Seismol. Soc. Am.* **114**, 726–740 (2023).
9. Liu, C. et al. Complex multi-fault rupture and triggering during the 2023 earthquake doublet in southeastern Türkiye. *Nat. Commun.* **14**, 5564 (2023).
10. Abdelmeguid, M. et al. Dynamics of episodic supershear in the 2023 M7.8 Kahramanmaraş/Pazarcik earthquake, revealed by near-field records and computational modeling. *Commun. Earth Environ.* **4**, 456 (2023).
11. Yao, S. & Yang, H. Rupture phases reveal geometry-related rupture propagation in a natural earthquake. *Sci. Adv.* **11**, eadq0154 (2025).
12. Bao, H. et al. Global frequency of oceanic and continental supershear earthquakes. *Nat. Geosci.* **15**, 942–949 (2022).
13. Passelègue, F. X., Schubnel, A., Nielsen, S., Bhat, H. S. & Madariaga, R. From sub-Rayleigh to supershear ruptures during stick-slip experiments on crustal rocks. *Science* **340**, 1208–1211 (2013).
14. Dunham, E. M. Conditions governing the occurrence of supershear ruptures under slip-weakening friction. *J. Geophys. Res. B: Solid Earth* **112**, B07302 (2007).
15. Xia, K., Rosakis, A. J. & Kanamori, H. Laboratory earthquakes: the sub-Rayleigh-to-supershear rupture transition. *Science* **303**, 1859–1861 (2004).
16. Bruhat, L., Fang, Z. & Dunham, E. M. Rupture complexity and the supershear transition on rough faults. *J. Geophys. Res. B: Solid Earth* **121**, 210–224 (2016).
17. Arpat, E. & Saroglu, F. The East Anatolian fault system: thoughts on its development. *Bull. Miner. Res. Explor.* **78**, 33–39 (1972).
18. Duman Tamer, Y. & Emre, Ö. The East Anatolian Fault: geometry, segmentation and jog characteristics. *Geol. Soc. London Special Publ.* **372**, 495–529 (2013).
19. Güvercin, S. E., Karabulut, H., Konca, A. Ö, Doğan, U. & Ergintav, S. Active seismotectonics of the East Anatolian Fault. *Geophys. J. Int.* **230**, 50–69 (2022).
20. Weiss, J. R. et al. High-resolution surface velocities and strain for Anatolia from Sentinel-1 InSAR and GNSS data. *Geophys. Res. Lett.* **47**, e2020GL087376 (2020).

21. Aktug, B. et al. Slip rates and seismic potential on the East Anatolian Fault System using an improved GPS velocity field. *J. Geodyn.* **94-95**, 1–12 (2016).
22. Zhao, D., Mishra, O. & Sanda, R. Influence of fluids and magma on earthquakes: seismological evidence. *Phys. Earth Planet. Inter.* **132**, 249–267 (2002).
23. Zhang, G., Li, Y. & Hu, X. Nucleation mechanism of the 2021 Mw 7.4 Maduo earthquake, NE Tibetan Plateau: insights from seismic tomography and numerical modeling. *Tectonophysics* **839**, 229528 (2022).
24. Mahesh, P., Gupta, S., Rai, S. & Sarma, P. R. Fluid driven earthquakes in the Chamoli Region, Garhwal Himalaya: evidence from local earthquake tomography. *Geophys. J. Int.* **191**, 1295–1304 (2012).
25. Boness, N. L. & Zoback, M. D. Mapping stress and structurally controlled crustal shear velocity anisotropy in California. *Geology* **34**, 825–828 (2006).
26. Zinke, J. C. & Zoback, M. D. Structure-related and stress-induced shear-wave velocity anisotropy: observations from microearthquakes near the Calaveras Fault in Central California. *Bull. Seismol. Soc. Am.* **90**, 1305–1312 (2000).
27. Audet, P. Layered crustal anisotropy around the San Andreas Fault near Parkfield, California. *J. Geophys. Res. B: Solid Earth* **120**, 3527–3543 (2015).
28. Li, Z. & Peng, Z. Stress- and structure-induced anisotropy in Southern California from two decades of shear wave splitting measurements. *Geophys. Res. Lett.* **44**, 9607–9614 (2017).
29. Crampin, S. Geological and industrial implications of extensive-dilatancy anisotropy. *Nature* **328**, 491–496 (1987).
30. Almqvist, B. S. & Mainprice, D. Seismic properties and anisotropy of the continental crust: predictions based on mineral texture and rock microstructure. *Rev. Geophys.* **55**, 367–433 (2017).
31. Cochran, E. S., Vidale, J. E. & Li, Y. G. Near-fault anisotropy following the Hector Mine earthquake. *J. Geophys. Res. B: Solid Earth* **108**, 2436 (2003).
32. Pei, S., Chen, Y. J., Feng, B., Gao, X. & Su, J. High-resolution seismic velocity structure and azimuthal anisotropy around the 2010 Ms=7.1 Yushu earthquake, Qinghai, China from 2D tomography. *Tectonophysics* **584**, 144–151 (2013).
33. Legendre, C. P., Zhao, L. & Tseng, T.-L. Large-scale variation in seismic anisotropy in the crust and upper mantle beneath Anatolia, Turkey. *Commun. Earth Environ.* **2**, 73 (2021).
34. Wang, H. et al. Isotropic and anisotropic P wave velocity structures of the crust and uppermost mantle beneath Turkey. *J. Geophys. Res. B: Solid Earth* **125**, e2020JB019566 (2020).
35. Mutlu, A. K. & Karabulut, H. Anisotropic Pn tomography of Turkey and adjacent regions. *Geophys. J. Int.* **187**, 1743–1758 (2011).
36. Medved, I., Polat, G. & Koulakov, I. Crustal structure of the Eastern Anatolia Region (Turkey) based on seismic tomography. *Geosciences* **11**, 91 (2021).
37. Güvercin, S. E. A local earthquake tomography on the EAF shows dipping fault structure. *Turk. J. Earth Sci.* **32**, 294–305 (2023).
38. Zhan, H. et al. The 2023 Turkey earthquake doublet: earthquake relocation, seismic tomography and stress field inversion. *Earth Planet. Phys.* **8**, 535–548 (2024).
39. Wang, Z., Qiu, Q., Fu, Y., Lin, J. & Pei, S. Distinct triggering mechanisms of the 2023 Türkiye earthquake doublet. *Commun. Earth Environ.* **6**, 287 (2025).
40. Xue, X. et al. Co-seismic P-wave velocity changes of 2023 Türkiye earthquake doublet. *Earthquake Sci.* **38**, 263–272 (2025).
41. Tong, P. Adjoint-state traveltime tomography for azimuthally anisotropic media and insight into the crustal structure of central California near Parkfield. *J. Geophys. Res. B: Solid Earth* **126**, e2021JB022365 (2021).
42. Chen, J., Chen, G., Nagaso, M. & Tong, P. Adjoint-state traveltime tomography for azimuthally anisotropic media in spherical coordinates. *Geophys. J. Int.* **234**, 712–736 (2023).
43. Tong, P., Li, T., Chen, J. & Nagaso, M. Adjoint-state differential arrival time tomography. *Geophys. J. Int.* **236**, 139–160 (2023).
44. Fuchs, S. & Norden, B. International heat flow commission. The global heat flow database: release 2021. *GFZ Data Services* https://doi.org/10.5880/fidgeo.2021.014 (2021).
45. Rojay, B., Heimann, A. & Toprak, V. Neotectonic and volcanic characteristics of the Karasu fault zone (Anatolia, Turkey): the transition zone between the Dead Sea transform and the East Anatolian fault zone. *Geodin. Acta* **14**, 197–212 (2001).
46. Agostini, S., Di Giuseppe, P., Manetti, P., Doglioni, C. & Conticelli, S. A heterogeneous subcontinental mantle under the African–Arabian Plate boundary revealed by boron and radiogenic isotopes. *Sci. Rep.* **11**, 11230 (2021).
47. Alici, P., Temel, A., Gourgaud, A., Vidal, P. & Gündogdu, M. N. Quaternary tholeiitic to alkaline volcanism in the Karasu Valley, Dead Sea rift zone, Southeast Turkey: Sr-Nd-Pb-O isotopic and trace-element approaches to crust-mantle interaction. *Int. Geol. Rev.* **43**, 120–138 (2001).
48. Bagherzadeh, P., Goshtasbi, K., Kazemzadeh, E., Kashef, M. & Aloki Bakhtiari, H. Stress-dependence of the permeability, porosity, and compressibility in fractured porous media regarding fracturing condition. *Bull. Eng. Geol. Environ.* **80**, 5091–5110 (2021).
49. Wu, S., Jiang, C., Schulte-Pelkum, V. & Tong, P. Complex patterns of past and ongoing crustal deformations in Southern California revealed by seismic azimuthal anisotropy. *Geophys. Res. Lett.* **49**, e2022GL100233 (2022).
50. Scholz, C. H. Earthquakes and friction laws. *Nature* **391**, 37–42 (1998).
51. Fulton, P. M. & Saffer, D. M. Potential role of mantle-derived fluids in weakening the San Andreas Fault. *J. Geophys. Res. B: Solid Earth* https://doi.org/10.1029/2008JB006087 (2009).
52. Kodaira, S. et al. High pore fluid pressure may cause silent slip in the Nankai Trough. *Science* **304**, 1295–1298 (2004).
53. Byerlee, J. Friction, overpressure and fault normal compression. *Geophys. Res. Lett.* **17**, 2109–2112 (1990).
54. Rice, J. R. in *International Geophysics* (eds Evans, B. & Wong, T.-F.) Vol. 51, 475–503 (Academic Press, 1992).
55. Cappa, F., Scuderi, M. M., Collettini, C., Guglielmi, Y. & Avouac, J.-P. Stabilization of fault slip by fluid injection in the laboratory and in situ. *Sci. Adv.* **5**, eaau4065 (2019).
56. Bürgmann, R. The geophysics, geology and mechanics of slow fault slip. *Earth Planet. Sci. Lett.* **495**, 112–134 (2018).
57. Gutierrez, M., Øino, L. & Nygaard, R. Stress-dependent permeability of a de-mineralised fracture in shale. *Mar. Pet. Geol.* **17**, 895–907 (2000).
58. Segall, P. & Rice, J. R. Dilatancy, compaction, and slip instability of a fluid-infiltrated fault. *J. Geophys. Res. B: Solid Earth* **100**, 22155–22171 (1995).
59. Li, J. et al. High seismic velocity structures control moderate to strong induced earthquake behaviors by shale gas development. *Commun. Earth Environ.* **4**, 188 (2023).
60. Xu, J., Zhang, H. & Chen, X. Rupture phase diagrams for a planar fault in 3-D full-space and half-space. *Geophys. J. Int.* **202**, 2194–2206 (2015).
61. Bao, H. et al. Early and persistent supershear rupture of the 2018 magnitude 7.5 Palu earthquake. *Nat. Geosci.* **12**, 200–205 (2019).
62. Weng, H. & Ampuero, J.-P. Continuum of earthquake rupture speeds enabled by oblique slip. *Nat. Geosci.* **13**, 817–821 (2020).
63. Nalbant, S. S., McCloskey, J., Steacy, S. & Barka, A. A. Stress accumulation and increased seismic risk in eastern Turkey. *Earth Planet. Sci. Lett.* **195**, 291–298 (2002).

64. Wessel, P. et al. The generic mapping tools version 6. *Geochem. Geophys. Geosyst.* **20**, 5556–5564 (2019).
65. Willemann, R. J. & Storchak, D. A. Data collection at the international seismological centre. *Seismol. Res. Lett.* **72**, 440–453 (2001).

Methods

Data collection and filtering

Our study region encompasses a volume of approximately 300 km × 600 km × 40 km, covering the entire rupture zone of the 2023 M_w 7.8 Turkey earthquake and its surrounding areas (Fig. 1). Earthquakes, seismic stations and the associated P-wave travel times spanning from January 2000 to August 2023 are downloaded from the International Seismological Center[65], resulting in an initial dataset of 489,988 travel times originating from 66,337 earthquakes and recorded by 95 stations.

To ensure the high quality of our dataset, we apply rigorous selection criteria. First, we retain only the first P-wave travel times with epicentre distances smaller than 100 km. This criterion aims to exclude travel time data that might be influenced by uncertainties in Moho topography. Second, we conduct linear regression analysis on the retained travel time data (Supplementary Fig. 1). Any travel time with a bias exceeding three times the standard estimated error (approximately 3 seconds) is excluded. Third, events with fewer than five records are discarded. Additionally, to mitigate the influence of source term uncertainties on the tomographic inversion, we incorporate common-source differential arrival times by catalogue subtraction. To enhance path overlapping on the source side, we restrict the separation of station pairs to within 100 km and constrain the angle difference between a common source and two selected stations to be less than 30°. Following these criteria, a total of 152,262 travel times and 81,815 common-source differential arrival times originating from 20,531 earthquakes and recorded by 92 stations are selected for the tomographic inversion (Fig. 2).

Adjoint-state travel time tomography and earthquake location

We employ the adjoint-state travel time tomography method[41–43] to image subsurface velocity heterogeneity and azimuthal anisotropy. This method aims to determine optimal model parameters $\mathbf{m}$, consisting of slowness $s(\mathbf{x})$ (reciprocal of velocity) and azimuthal anisotropic parameters $\xi(\mathbf{x})$, $\eta(\mathbf{x})$, by minimizing the discrepancy between synthetic and observed data

$$\min_{\mathbf{m}} \chi(\mathbf{m}) = \sum_{i=1}^{N_s}\sum_{m=1}^{N_r} \frac{w_{i,m}}{2}\left(T_{i,m}(\mathbf{m}) - T_{i,m}^{\mathrm{obs}}\right)^2 + \sum_{i=1}^{N_s}\sum_{m=1}^{N_r}\sum_{n=1}^{N_r} \frac{w_{i,m,n}}{2}\left(\Delta T_{i,m,n}(\mathbf{m}) - \Delta T_{i,m,n}^{\mathrm{obs}}\right)^2.$$

Here the first component of the right-hand side quantifies the difference between the synthetic travel time $T_{i,m}(\mathbf{m})$ and the observed one $T_{i,m}^{\mathrm{obs}}$ originating from the ith earthquake at $\mathbf{x}_{s,i}$ and recorded by the m th station at $\mathbf{x}_{r,m}$. The second component measures the difference between the synthetic common-source differential arrival time $\Delta T_{i,m,n}(\mathbf{m}) = T_{i,m}(\mathbf{m}) - T_{i,n}(\mathbf{m})$ and the observed one $\Delta T_{i,m,n}^{\mathrm{obs}} = T_{i,m}^{\mathrm{obs}} - T_{i,n}^{\mathrm{obs}}$. The weight coefficients $w_{i,m}$ and $w_{i,m,n}$ represent the existence and reliability of the data. Sensitivity kernels with respect to model parameters are computed based on the adjoint-state method

$$K_s(\mathbf{x}) = \sum_{i=1}^{N_s} P_i(\mathbf{x})\, s^2(\mathbf{x}),$$

$$K_\xi(\mathbf{x}) = \sum_{i=1}^{N_s} P_i(\mathbf{x})\left(\frac{1}{r^2}\left(\partial_\theta T_i(\mathbf{x})\right)^2 - \frac{1}{r^2\cos^2\theta}\left(\partial_\phi T_i(\mathbf{x})\right)^2\right),$$

$$K_\eta(\mathbf{x}) = \sum_{i=1}^{N_s} P_i(\mathbf{x})\left(-\frac{2}{r^2\cos\theta}\partial_\theta T_i(\mathbf{x})\,\partial_\phi T_i(\mathbf{x})\right),$$

where $T_i(\mathbf{x})$ and $P_i(\mathbf{x})$ are travel time field and adjoint field relative to the ith earthquake, respectively. This tomographic method utilizes the fasting sweeping method to solve anisotropic Eikonal equations for synthetic travel time fields[66]. It eliminates the potential inaccuracy in conventional shooting and bending methods for ray tracing[67,68], thereby facilitating accurate and reliable imaging results.

We solve this minimization problem using the step-size controlled gradient descent method[41,42]. At each iterative step, the model perturbation $(\frac{\delta s}{s}, \delta\xi, \delta\eta)$ is aligned with the negative gradient direction $(-K_s, -K_\xi, -K_\eta)$ and adjusted in scale. The maximum amplitude of model perturbation is set to be 1% in the first iteration and decreases once the objective function value increases in subsequent iterations, which ensures the convergence of the iteration process. Furthermore, we employ the multiple-grid parameterization method to discretize the model perturbation, which bolsters the robustness of the inversion[69].

Earthquake locations $\mathbf{x}_{s,i}$ and origin times τ_i are also updated during the inversion process, aiding in the mitigation of imaging artifacts arising from source term uncertainties. The derivatives of the travel time misfit with respect to earthquake location and origin time are given by

$$\mathbf{K}_{\mathbf{x}_{s,i}} = \sum_{m=1}^{N_r} w_{i,m}\left(T_{i,m}(\mathbf{m}) + \tau_i - T_{i,m}^{\mathrm{obs}}\right)\nabla\Gamma_m(\mathbf{x}_{s,i}),$$

$$K_{\tau_i} = \sum_{m=1}^{N_r} w_{i,m}\left(T_{i,m}(\mathbf{m}) + \tau_i - T_{i,m}^{\mathrm{obs}}\right),$$

in which $\Gamma_m(\mathbf{x})$ describes the travel time field originating from the m th station at $\mathbf{x}_{r,m}$. A step-size controlled gradient descend method is applied to iteratively update source terms[43,70], similar to the approach used for updating model parameters.

Inversion workflow

The inversion workflow consists of two stages: initial 1D isotropic model inversion and subsequent 3D anisotropic model inversion. In the first stage, we invert direct P travel times for an optimal 1D velocity model. The initial 1D model is constructed by horizontally averaging the Crust1.0 model in the study region[71] (Supplementary Fig. 2a). The mean value of travel time residuals in the initial model is −0.650 s (Supplementary Fig. 2b), which indicates the initial model is generally faster than that favoured by the data. After 15 iterations, the mean value of travel time residuals in the updated model approaches zero (0.036 s) (Supplementary Fig. 2b). The updated 1D velocity model (Supplementary Fig. 2a) serves as a suitable initial model for the subsequent 3D anisotropic model inversion.

In the second stage, we simultaneously invert travel times and common-source differential arrival times to determine subsurface 3D velocity heterogeneities and azimuthal anisotropies and source locations. Because the event catalogue is directly requested from a public data centre, uncertainties in the source term may potentially introduce artifacts to the final model. To mitigate this effect, we incorporate an additional source relocation step before the model and source updates. Subsequently, we alternatively update model parameters and source terms for 100 iterations to obtain the final model. The preliminary relocation process comprises 30 iterations. We observe that increasing the number of iterations slightly reduces the standard deviation of data residuals computed using the final inversion model (Supplementary Figs. 3c,d) while causing negligible changes to the main features that we discussed (Supplementary Figs. 3a,b). This finding suggests that our tomographic images are less susceptible to the initial source uncertainties, possibly due to the substantial data volume, the utilization of the common-source differential arrival times and/or the supplementary source relocation during the model and source updates.

Checkerboard resolution tests

We perform a checkerboard resolution test to assess data resolving capability. The target velocity model $v_T(\mathbf{x})$ is constructed by adding staggered velocity and anisotropic perturbations to the initial model

$v_0(\mathbf{x})$ above 20 km depth, where the earthquake rupture occurred (Supplementary Fig. 4a). The velocity perturbation has a form of

$$\frac{\Delta v_T(\mathbf{x})}{v_0(\mathbf{x})} = \frac{v_T(\mathbf{x}) - v_0(\mathbf{x})}{v_0(\mathbf{x})} = 3\% \sin\left(\pi \frac{\theta}{0.75^\circ}\right) \sin\left(\pi \frac{\phi}{0.75^\circ}\right) \sin\left(\pi \frac{z}{10\,\mathrm{km}}\right).$$

The azimuthally anisotropic parameters of the checkerboard model write

$$\xi_T(\mathbf{x}) = \epsilon(\mathbf{x}) \cos 2\psi(\mathbf{x}), \quad \eta_T(\mathbf{x}) = \epsilon(\mathbf{x}) \sin 2\psi(\mathbf{x}),$$

where the magnitude of anisotropy $\epsilon(\mathbf{x})$ and the fast velocity direction $\psi(\mathbf{x})$ are given by

$$\epsilon(\mathbf{x}) = 3\% \sin\left(\pi \frac{\theta}{1.00^\circ}\right) \sin\left(\pi \frac{\phi}{1.00^\circ}\right) \sin\left(\pi \frac{z}{10\,\mathrm{km}}\right),$$

$$\psi(\mathbf{x}) = \begin{cases} 60^\circ, & \epsilon(\mathbf{x}) < 0, \\ 150^\circ, & \epsilon(\mathbf{x}) \geq 0. \end{cases}$$

We compute synthetic travel times using the target model and add random Gaussian noise with a standard deviation of 0.1 s that simulates data noise. Common-source differential arrival times are computed using synthetic travel times. We perform the inversion with the initial model and update model parameters iteratively, ensuring that data configuration and inversion parameters remain consistent with those used in the real-data inversion.

After 100 iterations, the standard deviation of travel time residuals decreases from 0.138 to 0.100 s, comparable to the noise level. The staggered pattern of velocity and anisotropic anomalies is well recovered around the fault, which is the main focus of our study (Supplementary Fig. 4b). However, the amplitude of the recovered anomaly at 15-km depth is slightly underestimated, possibly due to a smaller number of earthquakes occurring at depths greater than 20 km. Overall, this checkerboard resolution test indicates a good resolving capability of our data for imaging the crustal structure beneath the EAF down to 15-km depth. To quantitatively delineate the well-resolved region, we introduce resolution functions $R_v(\mathbf{x})$ and $R_{ani}(\mathbf{x})$ that respectively measure the velocity and anisotropy discrepancies between the target model and the recovered model[72], given by

$$R_v(\mathbf{x}) = 1 - \frac{\int_{B(\mathbf{x})} (\Delta v(\mathbf{x}) - \Delta v_T(\mathbf{x}))^2 \mathrm{d}\mathbf{x}}{2\int_{B(\mathbf{x})} \Delta v(\mathbf{x})^2 + \Delta v_T(\mathbf{x})^2 \mathrm{d}\mathbf{x}},$$

$$R_{ani}(\mathbf{x}) = 1 - \frac{\int_{B(\mathbf{x})} (\xi(\mathbf{x}) - \xi_T(\mathbf{x}))^2 + (\eta(\mathbf{x}) - \eta_T(\mathbf{x}))^2 \mathrm{d}\mathbf{x}}{2\int_{B(\mathbf{x})} \xi(\mathbf{x})^2 + \eta(\mathbf{x})^2 + \xi_T(\mathbf{x})^2 + \eta_T(\mathbf{x})^2 \mathrm{d}\mathbf{x}}.$$

Here $B(\mathbf{x})$ is a small domain centred at $\mathbf{x}$ with a size of 0.5° × 0.5° × 10 km, comparable in size to the checkerboard anomaly. Higher values of $R_v(\mathbf{x})$ and $R_{ani}(\mathbf{x})$ indicate a more accurate recovery of the model around $\mathbf{x}$ (Supplementary Fig. 4c). We depict the contour of resolution functions at a threshold value of 0.7 and observe that it outlines the well-recovered region (Supplementary Fig. 4b). Therefore, this contour is used to determine the reliably resolved anomalies, beyond which the anomalies are masked in the imaging results of real-data inversion (Fig. 3).

To evaluate whether velocity and azimuthal anisotropy can be decoupled by our data, we perform an additional leakage test. The target model is constructed by assigning velocity perturbations to the initial model without adding any azimuthal anisotropy (Supplementary Fig. 5a). Then, we execute the same inversion procedure as used for the observed data, simultaneously inverting for velocity and anisotropy. In the recovered model (Supplementary Fig. 5b), velocity perturbations are accurately recovered, consistent with the results of the anisotropy-considered checkerboard test. Notably, the leakage from velocity anomalies to anisotropic anomalies is minor, less than 0.5% in most areas, indicating that velocity and azimuthal anisotropy can be effectively decoupled by our data. Thus, the anisotropic anomalies within the well-resolved region in our tomographic images are deemed reliable.

Data availability

The travel time catalogue was downloaded from the International Seismological Center[65] at https://www.isc.ac.uk/. The final anisotropic velocity model and the relocated catalogue can be accessed at https://doi.org/10.21979/N9/EANWVE.

Code availability

The seismic tomographic inversion was performed using the open-source package TomoATT[73] available at https://tomoatt.com/.

References

66. Luo, S. & Qian, J. Fast sweeping methods for factored anisotropic Eikonal equations: multiplicative and additive factors. *J. Sci. Comput.* **52**, 360–382 (2012).
67. Vidale, J. Finite-difference calculation of travel times. *Bull. Seismol. Soc. Am.* **78**, 2062–2076 (1988).
68. Rawlinson, N., Hauser, J. & Sambridge, M. Seismic ray tracing and wavefront tracking in laterally heterogeneous media. *Adv. Geophys.* **49**, 203–273 (2008).
69. Tong, P., Yang, D. & Huang, X. Multiple-grid model parametrization for seismic tomography with application to the San Jacinto fault zone. *Geophys. J. Int.* **218**, 200–223 (2019).
70. Tong, P. Adjoint-state traveltime tomography: Eikonal equation-based methods and application to the Anza area in Southern California. *J. Geophys. Res. B: Solid Earth* **126**, e2021JB021818 (2021).
71. Laske, G., Masters, G., Ma, Z. & Pasyanos, M. Update on CRUST1.0 - A 1-degree global model of Earth's crust. *Geophys. Res. Abstr.* **15**,EGU2013-2658 (2013).
72. Zelt, C. A. Lateral velocity resolution from three-dimensional seismic refraction data. *Geophys. J. Int.* **135**, 1101–1112 (1998).
73. Chen, J., Nagaso, M., Xu, M. & Tong, P. TomoATT: an open-source package for Eikonal equation-based adjoint-state traveltime tomography for seismic velocity and azimuthal anisotropy. *Comput. Geosci.* **204**, 105995 (2025).
74. Álvarez-Gómez, J. A. FMC: a one-liner Python program to manage, classify and plot focal mechanisms. *Geophys. Res. Abstr.* **16**, EGU2014–10887 (2014).
75. Álvarez-Gómez, J. A. FMC—earthquake focal mechanisms data management, cluster and classification. *SoftwareX* **9**, 299–307 (2019).

Acknowledgements

This research was sponsored by the Ministry of Education, Singapore, under its MOE AcRF Tier-2 grants (MOE-T2EP20124-0003, MOE-T2EP20122-0008, MOE-T2EP50124-0011 to P.T.) and partially supported by the Ministry of Education, Singapore, under its MOE AcRF Tier 3 grant (MOE-MOET32021-0002 to P.T.), 'Integrating Volcano and Earthquake Science and Technology (InVEST)'. This research was also supported by the National Key Research and Development Program of China (2023YFF0803202 to H.Y.), Hong Kong Research Grant Council grants (14308523, 14306122 to H.Y.) and the Faculty of Science, The Chinese University of Hong Kong (CUHK).

Author contributions

P.T. and J.C. conceived the study. M.N., J.C., M.X., S.H. and P.T. developed the adjoint-state travel time tomography code. J.C. processed the data, performed the tomography and drafted the manuscript. J.C. and Y.B. prepared the figures. All authors discussed the results and contributed to its revision.

Competing interests

The authors declare no competing interests.

Additional information

Extended data is available for this paper at https://doi.org/10.1038/s41561-025-01893-z.

Supplementary information The online version contains supplementary material available at https://doi.org/10.1038/s41561-025-01893-z.

Correspondence and requests for materials should be addressed to Ping Tong.

Peer review information *Nature Geoscience* thanks Thomas Ulrich and Metin Kahraman for their contribution to the peer review of this work. Primary Handling Editors: Tamara Goldin and Stefan Lachowycz, in collaboration with the *Nature Geoscience* team.

https://doi.org/10.1038/s41561-025-01893-z

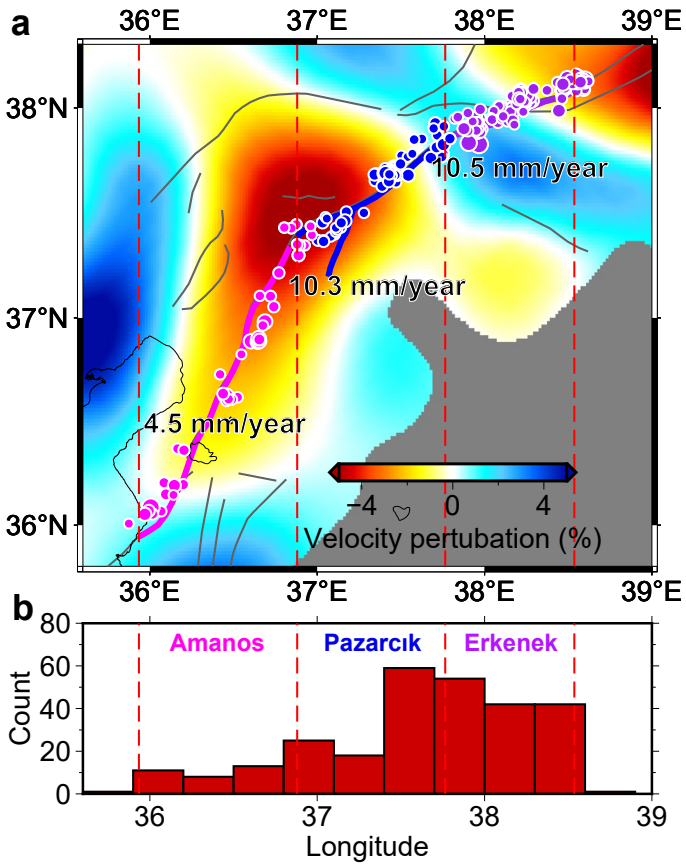

Extended Data Fig. 1 | Horizontal map of the earthquake distribution near the Eastern Anatolian Fault. a, Earthquakes with magnitude greater than 2.5 around the rupture zone during the period 2007-2019 are shown as circles[19]. The Amanos, Pazarcık, and Erkenek segments are highlighted by thick magenta, blue, and purple lines, respectively. Fault slip rates of the different segments are indicated[21]. **b**, Histogram of the earthquake count along the rupture zone. Basemap in **a** generated with Generic Mapping Tools[64].

https://doi.org/10.1038/s41561-025-01893-z

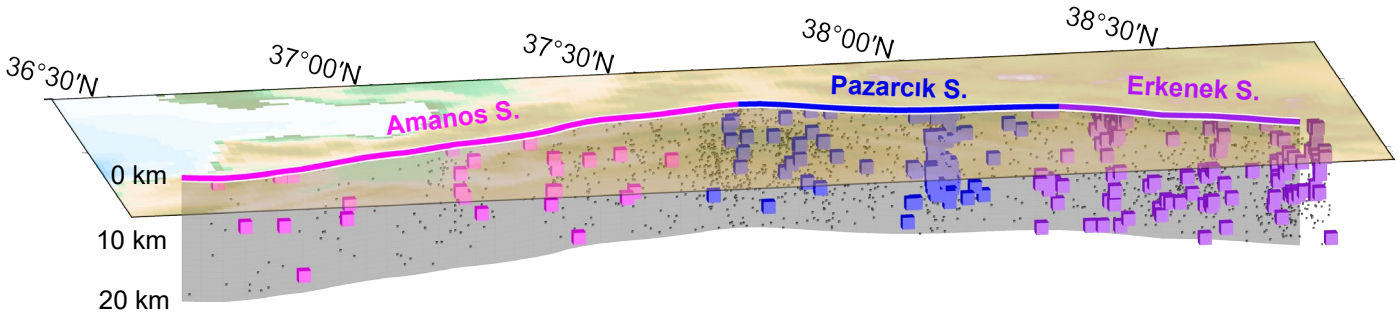

Extended Data Fig. 2 | Earthquake distribution near the Eastern Anatolian Fault. The earthquake data are from ref. 19, spanning the period 2007-2019. Earthquakes with magnitude greater than 2.5 are shown as color-coded cubes, while those with magnitude smaller than 2.5 are plotted as small black cubes. Basemap generated with Generic Mapping Tools[64].

https://doi.org/10.1038/s41561-025-01893-z

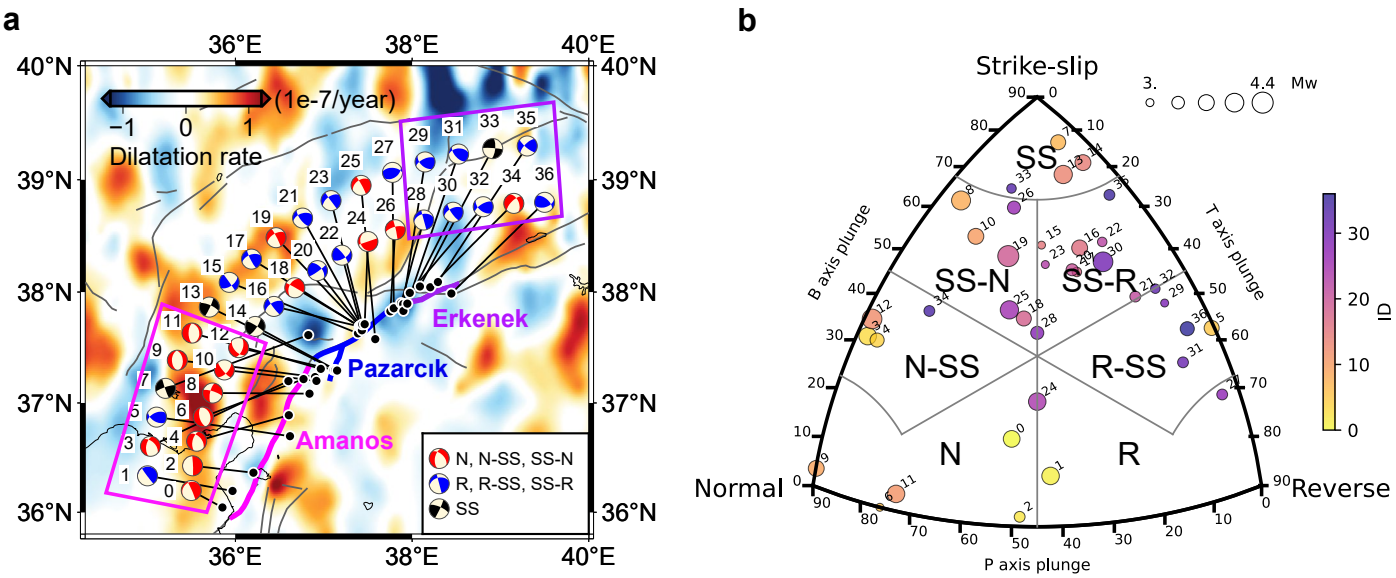

Extended Data Fig. 3 | Dilatation rate map and focal mechanisms of moderate earthquakes near the Eastern Anatolian Fault. a, The dilatation rate obtained from a joint inversion of GNSS and InSAR data[20] is depicted. Dilatational strain rates (positive values) are shown in red, while compressional strain rates (negative values) are shown in blue. The Amanos, Pazarcık, and Erkenek segments of EAF are highlighted by thick magenta, blue, and purple lines, respectively. Earthquakes[19] with magnitudes greater than 3.7 and occurring within 25 km of these segments are denoted by black dots. Their moment tensor solutions are also shown and color-coded based on the type of faulting determined by the FMC package[74,75]. N, N-SS, SS-N in red: normal, normal with strike-slip component, strike-slip with normal component; R, R-SS, SS-R in blue: reverse, reverse with strike-slip component, strike-slip with reverse component, and SS in black: strike-slip. **b**, The classification of the focal mechanism is presented[75]. Circles labeled with their IDs correspond to the moment tensor solutions depicted in (**a**). Basemap in **a** generated with Generic Mapping Tools[64].

https://doi.org/10.1038/s41561-025-01893-z

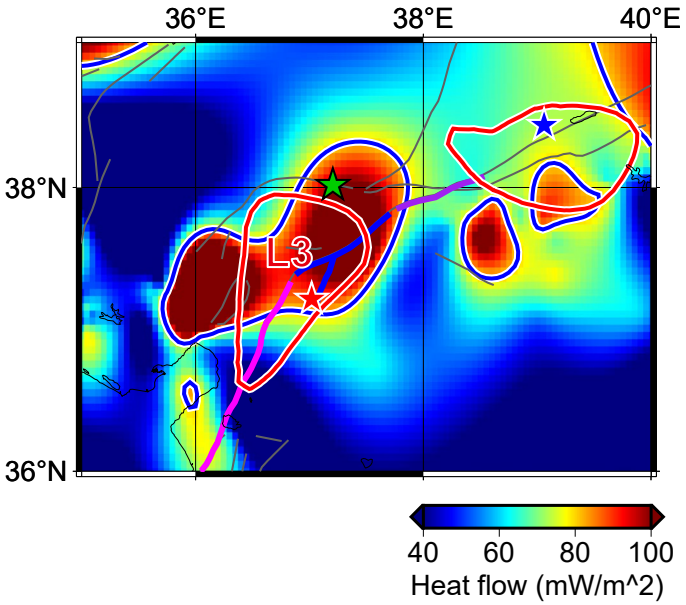

Extended Data Fig. 4 | Map of surface heat flow[44]. Red curves represent the -2% contour of velocity perturbation at 15 km depth. Within the northeast Amanos (magenta line) and Pazarcık segments (blue line), the low-velocity anomaly labeled as L3 corresponds to high heat flow exceeding 80 mW/m^2 (within blue curves). Basemap generated with Generic Mapping Tools[64].